



## Cobalt mixed oxides deposited on the SiC open-cell foams for nitrous oxide decomposition



A. Klegova<sup>1,\*</sup>, A. Inayat<sup>1</sup>, P. Indyka<sup>2</sup>, J. Grybos<sup>2</sup>, Z. Sojka<sup>2</sup>, K. Pacultová<sup>1</sup>, W. Schwieger<sup>3</sup>, A. Volodarskaja<sup>4</sup>, P. Kuśtrowski<sup>2</sup>, A. Rokicińska<sup>2</sup>, D. Fridrichová<sup>1,5</sup>, L. Obalová<sup>1</sup>

<sup>1</sup> Institute of Environmental Technology, VŠB – Technical University of Ostrava, 17. listopadu 15/2172, 708 00 Ostrava, Czech Republic

<sup>2</sup> Faculty of Chemistry, Jagiellonian University, Gronostajowa 2, 30-387 Krakow, Poland

<sup>3</sup> Institute of Chemical Reaction Engineering, Friedrich-Alexander-Universität Erlangen-Nürnberg, Egerland, 91058 Erlangen, Germany

<sup>4</sup> Faculty of Materials Science and Technology, VŠB – Technical University of Ostrava, 17. listopadu 15/2172, 708 00 Ostrava, Czech Republic

<sup>5</sup> Centre Energy Units for Utilization of Non Traditional Energy Sources, VŠB – Technical University of Ostrava, 17. listopadu 15/2172, 708 00 Ostrava, Czech Republic

### ARTICLE INFO

#### Keywords:

$\text{N}_2\text{O}$  decomposition  
Cobalt mixed oxide  
Open-cell foam  
Supported catalyst  
SiC

### ABSTRACT

Supported  $\text{Co}_3\text{O}_4$  and  $\text{Co}_4\text{MnAlO}_x$  mixed oxides were prepared by deposition on the SiC open-cell foams by wet impregnation and suspension methods and characterized by AAS, BET, XRD, SEM, TEM, TPR- $\text{H}_2$ , XPS and nitrogen adsorption methods. Prepared supported catalysts as well as active phase  $\text{Co}_3\text{O}_4$  and  $\text{Co}_4\text{MnAlO}_x$  in grain form prepared from parent solutions were tested for nitrous oxide decomposition. Catalytic activity of grain active phase was governed by methods of preparation;  $\text{Co}_3\text{O}_4$  and  $\text{Co}_4\text{MnAlO}_x$  prepared by suspension method were significantly more active than those from solutions for impregnation method. Suspension method provided active phase with higher surface areas and sites with better reducibility, both of these factors contributed to higher  $\text{N}_2\text{O}$  conversions. In contrast to this,  $\text{N}_2\text{O}$  conversions over supported catalysts were dependent more on chemical composition of active phase than on method of preparation. Both catalysts containing  $\text{Co}_4\text{MnAlO}_x$  mixed oxide revealed higher conversion of  $\text{N}_2\text{O}$  than catalysts containing  $\text{Co}_3\text{O}_4$ . STEM analysis of the most active  $\text{Co}_4\text{MnAlO}_x$  prepared by suspension method showed (i) segregation of  $\text{Co}_3\text{O}_4$  nanocrystals of cuboctahedral shape containing (100) and (111) facets (this segregation was confirmed also by XPS and TPR- $\text{H}_2$ ) and (ii) Co-Mn-Al oxide nanoparticles with very small un-faceted grains assembled into elongated fiber-like agglomerates were observed by STEM.

### 1. Introduction

Nitrous oxide ( $\text{N}_2\text{O}$ ) is considered as an important pollutant contributing to a greenhouse effect. The largest industrial sources of  $\text{N}_2\text{O}$  emissions are waste gases from nitric acid production plants [1]. The low-temperature catalytic decomposition of  $\text{N}_2\text{O}$  (up to 450 °C) to nitrogen and oxygen offers an attractive solution for decrease of  $\text{N}_2\text{O}$  emissions in tail gas from nitric acid production plants. Catalytic reactor for  $\text{N}_2\text{O}$  catalytic decomposition can be applied to the existing technologies and process does not require addition of a reducing agent. Important question is the choice of a suitable catalyst system. This catalyst must be active in the real waste gas conditions (in the presence of  $\text{O}_2$ ,  $\text{H}_2\text{O}$  and  $\text{NO}_x$ ), stable, sufficiently selective and relatively cheap.

Among tested catalysts, cobalt spinels such as  $\text{Co}_3\text{O}_4$  [2–8] and calcined layered double hydroxides (LDHs) containing cobalt Co [9], Co-Mg-Al [10], Co-Rh-Al [11], Co-Mn-Al [12–14] and Co-Cu [15] are

very promising for  $\text{N}_2\text{O}$  decomposition. To the best of our knowledge, only two research groups reported on manufacturing of shaped cobalt spinel based catalysts for low temperature  $\text{N}_2\text{O}$  decomposition in pilot plant scale conditions [16–18]. In both cases, the conventional packed beds with pelletized cobalt spinel based catalysts were used for  $\text{N}_2\text{O}$  decomposition. Disadvantage of this solution is that the catalytic reaction takes place only in a narrow surface region of the pellets due to internal diffusion limitation. This problem could be minimized by applying of a thin active layer deposited on the supporting material. Usage of supported catalysts allows reducing of needed amount of expensive and sometimes also harmful active components in the catalyst, which lowers their price and can increase mechanical strength of the catalyst. The support can be in form of differently shaped pellets or as structured support, which commonly consists of ceramic or metallic substrates pre-shaped in the form of a single continuous structure with stable geometry. Supported cobalt oxide de $\text{N}_2\text{O}$  catalysts were studied mainly on

\* Corresponding author.

E-mail address: [anna.klegova@vsb.cz](mailto:anna.klegova@vsb.cz) (A. Klegova).

different monoliths [19–22] or sieves [23,24] and also tablets [25,26]. However, most published results were obtained over grained samples in kinetic regime [27–32].

Nowadays, there is a growing interest in the potential of open-cell foam (or sponge) as novel structured catalysts/reactors [33–35].

Reticulated open-cell foam consists of an assembly of solid struts connected to each other three dimensionally to enclose cells of irregular shape. These cells communicate with each other via open windows. The foam structure can be described by its morphological parameters, namely cell and window diameter, strut diameter and porosity [36]. The foam structure exhibits different strut morphologies, namely cylindrical, triangular and triangular concave [37], depending on the porosities. The strut morphology greatly influences the specific surface area and consequently the heat and mass transfer, and the pressure drop of the foam structures. Open-cell foams (ceramic or metal) offer remarkable properties such as a large external surface area, a high mechanical strength, a high porosity and a low resulting pressure drop. For the application of foam structures as catalyst support, the knowledge of their specific surface area and their pressure drop properties is extremely important. These properties were studied by different authors [37–42] who presented various models and correlations for the specific surface area and the pressure drop determination.

Twigg and Richardson [43] have summarized work on the use of foams as catalyst supports for ammonia oxidation, catalytic combustion, partial oxidation, steam reforming, exhaust catalysis, and solar-driven methane-CO<sub>2</sub> reforming. Further work has appeared on foam supported catalysts for methane [44] or propane [45] combustions, steam-biogas reforming [46,47], catalytic wet peroxide oxidation [48,49].

The performance of foam catalysts for nitrous oxide decomposition has not been published in available literature yet.

Important question is the choice of a suitable method for active phase deposition. There are a lot of methods which can be used in order to deposit a thin catalyst layer on a structured surface, depending on the properties of the surface and deposited active phase. Impregnation method from salts solution of corresponding metals represents the most widely used and the simplest method of metal oxide deposition on all kinds of supports. This method is often used for preparation of supported catalyst in the form of grains [28], tablets [24], monoliths [19] and also foams [50,51]. Suspension method and sol-gel are the most often used methods for deposition of metal oxides on the monolith or foam. However, the difference between these two methods is tiny because the suspension method often implies some jellification steps. All methods based on the dispersion of a finished material have been gathered under the term suspension method. Powder (catalyst), binder, acid and water are the standard ingredients [52].

On the basis of the above mentioned facts, we decided to use foam supported catalysts also for N<sub>2</sub>O decomposition. The SiC foam was chosen as first possibility due to its stability at applied temperatures and chemical inertness. The aims of our work were: (i) deposition of known active phase (Co<sub>3</sub>O<sub>4</sub>, Co<sub>4</sub>MnAlO<sub>x</sub>), which were described in [4,6,10,27,53,54], on foam support by wet impregnation and suspension methods; (ii) testing of these catalysts for N<sub>2</sub>O decomposition; (iii) evaluation of the effects of deposition procedure on the physicochemical properties and deN<sub>2</sub>O activity of prepared catalyst.

## 2. Experimental

### 2.1. Preparation of cobalt mixed oxide deposited on open-cell foams

Catalysts were prepared by deposition of Co<sub>3</sub>O<sub>4</sub> and Co<sub>4</sub>MnAlO<sub>x</sub> on the silicon carbide foam (SiC, Fraunhofer IKTS, Dresden) with porosity of 20 ppi by wet impregnation and suspension methods.

For *wet impregnation method*, cobalt solution was prepared by dissolving of Co(NO<sub>3</sub>)<sub>2</sub> or Co(NO<sub>3</sub>)<sub>2</sub> + Al(NO<sub>3</sub>)<sub>3</sub> + Mn(NO<sub>3</sub>)<sub>2</sub> in distilled water at 60 °C. Open-cell (length 2 cm, diameter 3 cm) were cleaned by

acetone, weighted and heated to 75 °C before impregnation. Foams were dipped in cobalt nitrates or cobalt/manganese/alumina nitrates solution for 15–30 minutes. Then the samples were dried for 3 hours at 115 °C and calcined for 4 hours at 500 °C. The deposition procedure was repeated 3 times for achieving of higher amount of active phase on the foam. The prepared catalysts were denoted as Co<sub>3</sub>O<sub>4</sub>/SiC-w.i. and Co<sub>4</sub>MnAlO<sub>x</sub>/SiC-w.i.

For *suspension method*, at first Co(OH)-β and Co<sub>4</sub>MnAl(OH)<sub>x</sub>(CO<sub>3</sub>)<sub>y</sub> precursors were prepared. Co<sub>4</sub>MnAl(OH)<sub>x</sub>(CO<sub>3</sub>)<sub>y</sub> with the Co:Mn:Al molar ratio of 4:1:1 was prepared by co-precipitation of the corresponding nitrate solution in an alkaline Na<sub>2</sub>CO<sub>3</sub>/NaOH solution at 25 °C and pH 10. Co(OH)-β was prepared by co-precipitation of cobalt nitrate and sodium hydroxide aqueous solution. The resulting suspension was vigorously stirred at room temperature for 5 min. Then the products were filtered off, thoroughly washed with distilled water and dried at 70 °C in air. 5 g of powder of Co(OH)<sub>2</sub> or Co<sub>4</sub>MnAl(OH)<sub>x</sub>(CO<sub>3</sub>)<sub>y</sub> was milled with 10 g of water and with 100 g of ZrO<sub>2</sub> balls (3 mm) (Planetary Ball Mill PM 100, Retsch). Particle size was controlled by laser diffraction (Malvern Instruments). Distribution of particles size before and after milling was as follows, 90% of Co<sub>4</sub>MnAl(OH)<sub>x</sub>(CO<sub>3</sub>)<sub>y</sub> particles had initially diameter less than 436 μm (D (90%)), which was decreased to 12 μm by milling. Similarly, reduction of particle size from 394 μm (D (90%)) to 5.1 μm for Co(OH)<sub>2</sub>-β was observed. Two “colloid” solutions containing about 3 wt. % of Co(OH)-β and Co<sub>4</sub>MnAl(OH)<sub>x</sub>(CO<sub>3</sub>)<sub>y</sub> were prepared from prepared slurries. Deposition of active phase on the foam structure was performed by dip coating method with definite rate of immersion (0.5 mm/s). The foams were cleaned by acetone and weighted before coating. The foam was dipped into solution 10 times and then it was dried at 75 °C. The deposition procedure was repeated 3 times for achieving of higher amount of active phase on the foam. Then the samples were calcined for 4 hours at 500 °C. The catalysts were denoted as Co<sub>3</sub>O<sub>4</sub>/SiC-s.m. and Co<sub>4</sub>MnAlO<sub>x</sub>/SiC-s.m.

### 2.2. Characterization of prepared catalysts

Characterization of the active phase was performed on the powder obtained by drying (24 hours at 115 °C) and calcination (4 h at 500 °C) of the parent suspension/solution (the marking Co<sub>3</sub>O<sub>4</sub>-s.m., Co<sub>3</sub>O<sub>4</sub>-w.i., Co<sub>4</sub>MnAlO<sub>x</sub>-s.m. and Co<sub>4</sub>MnAlO<sub>x</sub>-w.i. is used) or on the crushed and sieved foam coated samples (fraction < 0.16 mm).

XRD patterns of catalysts were obtained using Rigaku SmartLab diffractometer (Rigaku, Japan) with detector D/teX Ultra 250. The source of X-ray irradiation was Co tube (CoK $\alpha$ ,  $\lambda_1 = 0.178892$  nm,  $\lambda_2 = 0.179278$  nm) operated at 40 kV and 40 mA. Incident and diffracted beam optics were equipped with 5 °Soller slits; incident slits were set up to irradiate the area of the sample 10 x 10 mm (automatic divergence slits) constantly. Slits on the diffracted beam were set up to fixed values 8 and 14 mm. The powder samples were gently grinded using agate mortar before analysis, pressed using microscope glass in rotational sample holder, and measured in the reflection mode (Bragg-Brentano geometry). The samples rotated (30 rpm) during the measurement to eliminate preferred orientation effect. The XRD patterns were collected in a 2θ range 5° - 90° with a step size of 0.01° and speed 0.5 deg.min<sup>-1</sup>. Measured XRD patterns were evaluated using PDXL 2 software (version 2.4.2.0) and compared with database PDF-2, release 2015.

Surface areas of the catalysts were determined by N<sub>2</sub> adsorption/desorption at -196 °C using QuadraSorb and evaluated by BET method. Prior to the measurements, the samples were dried at 250 °C for at least 12 h.

The chemical composition of prepared catalysts was determined by atomic absorption spectroscopy (AAS) using a SpectrAA880 instrument (Varian) after dissolving the samples in hydrochloric acid.

Temperature programmed reduction by hydrogen (TPR-H<sub>2</sub>) was carried out on AutoChemII 2920 (Micromeritics, USA). Prior to the TPR experiments, the samples were outgassed in the flow of pure argon

(50 ml min<sup>-1</sup>) at 450 °C for 60 min, cooled down in the same atmosphere. Afterwards, the TPR runs were performed in the flow of 10 mol % H<sub>2</sub>/Ar (50 ml min<sup>-1</sup>) with the heating rate 20 °C min<sup>-1</sup> in the temperature range 25 – 990 °C. The cold trap (-78 °C) was applied for elimination of water evolved during experiments. For the measurement, the sieve fraction < 0.16 mm was used.

Scanning electron microscopy with Quanta FEG 450 (FEI) with EDS analysis APOLLO X (EDAX) was used as microscopic method for characterization of morphology of the studied samples. Images were taken by use of secondary electrons and backscattered electrons detectors at 15 kV.

Transmission electron microscopy (TEM) measurements were carried out using a Tecnai Osiris instrument (FEI) with X-FEG Schottky field emitter operated at accelerating voltage of 200 kV to evaluate the morphology, phase and chemical composition of the Co<sub>3</sub>O<sub>4</sub> and Co<sub>4</sub>MnAlO<sub>x</sub> nanoparticles prepared by the suspension method on the SiC foams. Spatially resolved information on the sample element repartition was obtained by EDX using a Super-X EDX (Energy Dispersive X-ray) windowless detector system with 4-sector silicon drift detector (SDD) and Bruker Esprit software. The Z-contrast imaging was performed using a High Angle Annular Dark Field (HAADF) detector in the scanning mode. The camera length was kept in the range 330–550 mm, to maximize the HAADF signal intensity. Samples for TEM characterization were ultrasonically dispersed in ethanol, dropped into a lacey carbon-coated copper grid (Agar Scientific, 300 mesh), and dried at room temperature.

The cobalt spinel particle size analysis was performed using the DigitalMicrograph (Gatan) software [55]. Phase analysis of the samples was carried out by means of selected area electron diffraction (SAED). For clarity of the indexation, the acquired electron diffraction (ED) ring patterns were radially integrated into the intensity distribution, and after nonlinear background correction, presented as a function of the scattering angle using the Process Diffraction software [56]. The Debye-Scherrer ring simulations for the investigated phases were plotted using the crystal file data and the microscope ED experimental settings. For the simulation of the intensity of powder patterns (vertical markers indicating the peak positions in terms of interplanar values of the corresponding crystallographic phases), the Blackman dynamical correction implemented in JEMS software was used, in order to account better for the dynamical diffraction nature of ED. The nanocrystals shape retrieving was based on the gradient analysis of the HAADF images performed by means of the Canny algorithm [57] implemented in the *FeatureJ* [58] software as a part of the image processing software *ImageJ* [59]. The imaging conditions were adjusted in such way that the image contrast originated mainly from the changes in the thickness of the examined nanocrystals. As a result, by combining the knowledge about the sample structure with the information about the sample thickness variation and the edge pattern revealed owing to gradient representation of the acquired images, it was possible to retrieve the shape of nanocrystals by using a reversed Wulff construction [60]. X-ray photoelectron spectra were recorded by a hemispherical VG SCIENTA R3000 analyzer with constant pass energy of 100 eV and a monochromatized aluminum source Al K  $\alpha$  ( $E = 1486.6$  eV) and a low energy electron flood gun (FS40A-PS) to compensate the charge on the surface of nonconductive samples. The base pressure in the analytical chamber during the measurements was  $5 \times 10^{-9}$  mbar. The binding energies were referenced to the C 1s core level ( $E_b = 284.6$  eV). The composition and chemical surrounding of the sample surface were determined on the basis of the areas and binding energies of Co 2p, Mn 2p, Al 2p, Si 2p, O 1s and C 1s photoelectron peaks. The fitting of high resolution spectra was obtained through the Casa XPS software (version 2.3.16 PR 1.6).

### 2.3. Catalytic measurements

N<sub>2</sub>O catalytic decomposition was performed in integral fixed bed stainless steel reactor in the temperature range from 300 to 450 °C and

at atmospheric pressure. The feed introduced to the reactor contained 0.1 mol % N<sub>2</sub>O in N<sub>2</sub> and IR analyzer (Sick) was used for N<sub>2</sub>O analysis. Testing of the grained catalysts was performed in reactor with internal diameter of 5.5 mm and foam catalysts were tested in reactor with internal diameter of 30 mm. Grained catalyst bed contained 0.1 g of sample with particle size of 0.160 – 0.315 mm. The total gas flow of 100 ml/min (20 °C, 101 kPa) was used corresponding to WHSV of 60 m<sup>3</sup> kg<sup>-1</sup> h<sup>-1</sup>. Foam catalyst bed contained 14 cm<sup>3</sup> (length 2 cm, diameter 3 cm) of sample; the total gas flow of 700 ml/min (20 °C, 101 kPa) was used corresponding to GHSV of 3 000 m<sup>3</sup> m<sub>bed</sub><sup>-3</sup> h<sup>-1</sup>.

The application of the experimental tests to check the presence of external mass transfer limitation [61] revealed that this restraint was absent at given experimental conditions. No effect of internal diffusion on the reaction rate was also confirmed based on the thin of active phase layer (4–40  $\mu$ m) which is much thinner than diameter of grains (0.16–0.315 mm) used for catalytic tests. Internal diffusion in the cobalt based catalyst in grain form with size 0.16–0.315 mm was excluded in the work [17].

## 3. Results and discussion

### 3.1. Preparation and characterization of catalysts

Chemical composition and the amount of active phase deposited on the foam are shown in Table 1. Samples with the same type of active phase, Co<sub>3</sub>O<sub>4</sub> and Co<sub>4</sub>MnAlO<sub>x</sub>, show its similar loading about 14 and 12 wt. %, respectively.

The chemical analysis and specific surface area of prepared active phases are summarized in Table 2. Samples with the same type of active phase (Co<sub>3</sub>O<sub>4</sub> or Co<sub>4</sub>MnAlO<sub>x</sub>) show the same chemical composition. The molar ratios Co : Mn : Al calculated from the concentrations measured by AAS are close to those set during the preparation procedure. Using different methods of preparation and different precursors led to the formation of active phases with different textural properties. Samples prepared by suspension method showed higher BET surface area compared to wet impregnation method and simultaneously samples containing Al and Mn have higher surface area than samples containing only Co.

Results of XRD are summarized in Fig. 1 and Table 3. The X-ray diffraction lines characteristic for a cobalt spinel structure were indexed within the Fd3m space group and the diffractograms proved spinel structure in all investigated samples. SiC and graphite from the support was also found in the powder XRD pattern of the supported catalysts, together with the spinel phase. The mean coherence lengths Lc corresponding approximately to crystallite size were determined from half-width of peak spinel (311) using Scherrer's equation. The increase of crystallite size of active phase in order Co<sub>4</sub>MnAlO<sub>x</sub>-s.m. < Co<sub>4</sub>MnAlO<sub>x</sub>-w.i. < Co<sub>3</sub>O<sub>4</sub>-s.m. < Co<sub>3</sub>O<sub>4</sub>-w.i. was observed. Crystallite size corresponds with the determined surface area, the smaller the crystallite size the larger the surface area is. Crystallite size of active phase deposited on SiC foams have the same order and are similar with bulk samples (powder from parent solution). The order of surface area values (Table 2) remained the same even after the deposition of active phase

Table 1

Chemical composition and loading of active phase Co<sub>3</sub>O<sub>4</sub> and Co<sub>4</sub>MnAlO<sub>x</sub> in prepared foam catalysts.

Sample/Parameter	Co <sub>3</sub> O <sub>4</sub> /SiC-w.i.	Co <sub>4</sub> MnAlO <sub>x</sub> /SiC-w.i.	Co <sub>3</sub> O <sub>4</sub> /SiC-s.m.	Co <sub>4</sub> MnAlO <sub>x</sub> /SiC-s.m.
Total amount of active phase (g)	0.7921	0.6397	0.7529	0.5707
Total amount of active phase (wt.%)	14.2	12.5	13.8	11.9
Co (wt.%)	10.2	6.2	10.2	5.9
Mn (wt.%)	-	1.4	-	1.3

**Table 2**

Chemical composition and textural properties of active phase  $\text{Co}_3\text{O}_4$  and  $\text{Co}_4\text{MnAlO}_x$ , determined on powder obtained by drying and calcination of parent suspension/solution.

Sample/Parameter	$S_{\text{BET}}$ ( $\text{m}^2 \cdot \text{g}^{-1}$ )	$V_p^a$ ( $\text{cm}^3/\text{g}$ )	Co (wt. %)	Mn (wt. %)	Al (wt. %)	Co:Mn:Al molar ratio
$\text{Co}_3\text{O}_4\text{-w.i.}$	9	0.08	72.0	-	-	-
$\text{Co}_3\text{O}_4\text{-s.m.}$	19	0.35	73.8	-	-	-
$\text{Co}_4\text{MnAlO}_x\text{-w.i.}$	36	0.11	49.8	11.5	5.1	4.0 : 1.0 : 0.9
$\text{Co}_4\text{MnAlO}_x\text{-s.m.}$	99	0.73	49.7	10.6	5.7	4.0 : 0.9 : 1.0

<sup>a</sup> Total pore volume at  $p/p_0 = 0.994$ .

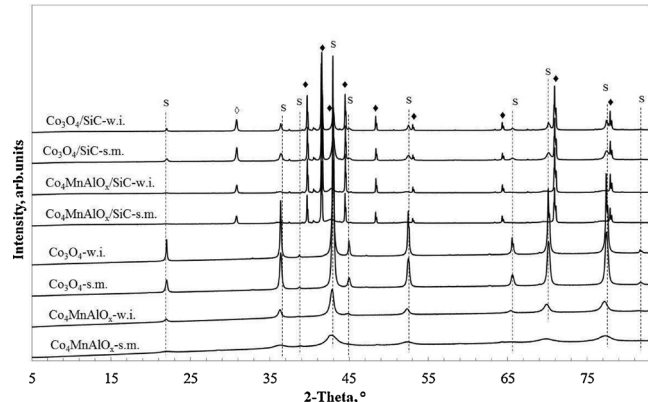


**Fig. 1.** XRD patterns of the prepared foam catalysts and unsupported active phases. Identified phases S – spinel phase,  $\blacklozenge$  – SiC,  $\lozenge$  – Graphite.

**Table 3**

Mean coherence lengths and lattice parameters of the active phase  $\text{Co}_3\text{O}_4$  and  $\text{Co}_4\text{MnAlO}_x$ .

Sample/ XRD parameter	$L_c$ (nm)	$a$ (nm)
$\text{Co}_3\text{O}_4\text{-w.i.}^*$	69	0.8073
$\text{Co}_3\text{O}_4\text{-s.m.}^*$	26	0.8073
$\text{Co}_4\text{MnAlO}_x\text{-w.i.}^*$	21	0.8103
$\text{Co}_4\text{MnAlO}_x\text{-s.m.}^*$	7	0.8156
$\text{Co}_3\text{O}_4/\text{SiC-w.i.}$	58	0.8073
$\text{Co}_3\text{O}_4/\text{SiC-s.m.}$	30	0.8076
$\text{Co}_4\text{MnAlO}_x/\text{SiC-w.i.}$	19	0.8109
$\text{Co}_4\text{MnAlO}_x/\text{SiC-s.m.}$	15	0.8096

\* Determined on powder obtained by drying and calcination of parent suspension/solution.

on the SiC support. Values of cell parameters of deposited samples did not change after deposition on SiC except for  $\text{Co}_4\text{MnAlO}_x/\text{SiC-s.m.}$ , which could be connected with larger structural changes reflected also in larger change of crystallite size after active phase deposition.

The morphology of cobalt mixed oxides deposited on SiC foams by different methods was studied by scanning electron microscopy and compared with active phase in grained form obtained from parent solutions. Micrographs of pure SiC foam and SiC with  $\text{Co}_3\text{O}_4$  active phase deposited by both methods are shown in Fig. 2. Deposition of active phase from nitrates solution by impregnation led to the formation of thin, smooth surface without cracks (Fig. 2b).

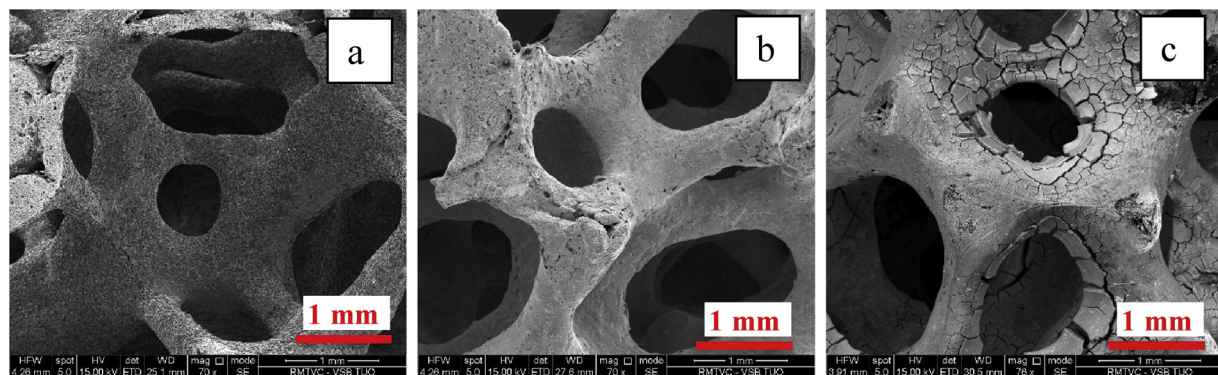
Deposition of active phase from suspension solution from calcined hydroxides or layered hydroxides led to the formation of thicker catalyst layers with cracks that may cause active phase loss during manipulation (Fig. 2c). Micrographs of catalysts in grain form (from parent solutions) and active phases deposited on SiC foams are shown in Fig. 3. The morphology of  $\text{Co}_3\text{O}_4$  is different in comparison with the

morphology of  $\text{Co}_4\text{MnAlO}_x$ , when the wet impregnation method was used. Surprisingly, samples prepared by suspension method have similar morphology despite their different chemical composition. The morphology of active phase deposited on the SiC is close to the corresponding bulk active phase. Mean size of the deposited active phase layers thickness is presented in Table 4. Thickness was measured in the cut of samples in 3 different places. Variation in the thickness of the active phase layers of samples with similar loadings of active phase (Table 1) is related to the different density of the obtained spinel. Differences in density could be connected with differences of pore volumes of the active phase (Table 2). Samples prepared by wet impregnation method contain lower volume of pores and thinner thickness in comparison to samples prepared by suspension method. The thinnest catalytic layer (4  $\mu\text{m}$ ) was detected over the  $\text{Co}_4\text{MnAlO}_x/\text{SiC-w.i.}$  sample.

SEM, XRD and textural results showed that active phase deposited by different methods has different morphology. The reason of the observed differences for samples with the same chemical compositions prepared by different methods is a different course of the crystallization process due to different temperature of precursors' decomposition, since different precursors were used for impregnation and suspension method. Such a finding is in good agreement with our previous work [13], where calcination of metal nitrates led to the formation of catalyst with higher crystallite size related to higher ordering of the crystal structure and lower surface area since well-crystallized samples are less porous.

Nano morphology of cobalt active phase deposited on the support from nitrate precursors was in detail studied by Sojka group [7,8,25]. Therefore, to continue the study of cobalt nanoparticles in this work, two different cobalt active phases  $\text{Co}_3\text{O}_4$  and  $\text{Co}_4\text{MnAlO}_x$  deposited on the SiC foam by suspension method were described by TEM analysis. The TEM and STEM observations revealed the presence of catalyst active phase nanoparticles of various extent of agglomeration, decorating the micrometer-size SiC foam support (Fig. 4a<sub>1</sub>, a<sub>3</sub>, b<sub>1</sub>, b<sub>3</sub>). In the case of  $\text{Co}_3\text{O}_4/\text{SiC-s.m.}$  sample, formation of nearly equant and slightly elongated well-shaped nanoparticles of an average particle size of ~20–50 nm was observed (Fig. 4a<sub>2</sub>). The  $\text{Co}_4\text{MnAlO}_x/\text{SiC-s.m.}$  sample exhibited less defined morphology consisting of much smaller ~3–5 nm grains assembled into loosely bound elongated fiber-like nanostructures (Fig. 4b<sub>2</sub>). A minor part of the cobalt was, however, segregated into cobalt spinel particles and characterized by much larger average grain size of ~20–50 nm. A comprehensive shape analysis of such nanocrystals for both samples is presented in the next paragraph.

The corresponding nanoscale EDX maps reported in Fig. 4a<sub>4</sub>, b<sub>4</sub> show redistribution of the constituent elements within the investigated samples (K<sub>α</sub> - lines): O (blue), Co (green), Si (red), C (grey), Mn (yellow), Al (orange), indicating the presence of  $\text{Co}_3\text{O}_4$  in  $\text{Co}_3\text{O}_4/\text{SiC-s.m.}$  cobalt mixed oxide sample and  $\text{Co}_3\text{O}_4$  together with Co–Mn–Al oxide nanoparticles in  $\text{Co}_4\text{MnAlO}_x/\text{SiC-s.m.}$  sample. Composition was inferred from a more detailed quantitative analysis of the EDX line profiles (Fig. 4a<sub>7</sub>, b<sub>7</sub>), where the signal was integrated along the line-scan direction marked in Fig. 4a<sub>4</sub>, b<sub>4</sub>. But these results are true on a very local scale. EDX analysis in different places show that chemical composition of Co–Mn–Al oxide nanoparticles is not homogeneous and molar ratio of Co:Mn:Al varies in range 4:0.7–1.1:0.3–0.8. EDX experiments on SEM were performed to find out stoichiometry in  $\text{Co}_4\text{MnAlO}_x/\text{SiC-s.m.}$  sample in larger scale. These results also indicate nonhomogeneous chemical composition of Co–Mn–Al oxide, in particular the nonhomogeneous content of aluminium in the mixed oxide. As a result, the molar ratio of Co:Mn:Al in investigated places varies in range 4:0.9–1.1:1–1.9. The TEM analysis confirmed that the  $\text{Co}_3\text{O}_4$  spinel stoichiometry of the nanoparticles in  $\text{Co}_3\text{O}_4/\text{SiC-s.m.}$  sample was well preserved, in line with the SEAD pattern diagnostic of the spinel phase (Fig. 4a<sub>5</sub>). The SEAD pattern of the  $\text{Co}_4\text{MnAlO}_x/\text{SiC-s.m.}$  catalyst exhibits only the peaks characteristic of the cobalt oxide structure (Fig. 4b<sub>5</sub>).

Fig. 2. SEM micrographs of a) pure foam, b)  $\text{Co}_3\text{O}_4/\text{SiC-w.i.}$  and c)  $\text{Co}_3\text{O}_4/\text{SiC-s.m.}$ 

As already mentioned, local segregation of cobalt was found in the  $\text{Co}_4\text{MnAlO}_x/\text{SiC-s.m.}$  sample, giving rise to formation of  $\text{Co}_3\text{O}_4$  nanoparticles (Fig. 4b<sub>7</sub>). Minor abundance of the Si and Zr oxide impurities were also detected in both samples (not shown). The selected area electron diffraction patterns show polycrystalline nature of the samples (Fig. 4a<sub>5</sub>, b<sub>5</sub>), where the Debye-Scherrer full-ring overlays substantiate the presence of the corresponding phases:  $\text{Co}_3\text{O}_4$  (*Fd3m*) in green,  $\text{SiC}$  (*P 63*) in red, and C (*P 63 mc*) in orange. In Fig. 4a<sub>6</sub>, b<sub>6</sub> the integrated ring intensities are plotted as a function of the scattering angle, and the vertical markers indicate peak positions of the identified crystallographic phases. An adventitious presence of the graphitized carbon in the investigated samples can be associated with its existence as a by-product in the parent SiC foam, used as a support.

Within the properly adjusted imaging conditions the intensity of the HAADF-STEM image depends on the sample thickness and the average atomic number of the projected atomic columns. Such HAADF-STEM images may be used, therefore, to assess the shape of the well-developed cobalt spinel nanocrystals. However, whereas the larger  $\text{Co}_3\text{O}_4$  nanocrystals are rather well faceted, the grains of Co-Mn-Al oxide nanoparticles, being much smaller, are agglomerated into less defined fiber-like superstructures. Thus, in the case of the  $\text{Co}_4\text{MnAlO}_x/\text{SiC-s.m.}$

Table 4

Mean size of thickness of deposited  $\text{Co}_3\text{O}_4$  or  $\text{Co}_4\text{MnAlO}_x$  layers.

	$\text{Co}_3\text{O}_4/\text{SiC-w.i.}$	$\text{Co}_4\text{MnAlO}_x/\text{SiC-w.i.}$	$\text{Co}_3\text{O}_4/\text{SiC-s.m.}$	$\text{Co}_4\text{MnAlO}_x/\text{SiC-s.m.}$
Thickness of active phase layer (μm)	15	4	40	31

samples, the shape analysis was restricted to the morphology of the segregated  $\text{Co}_3\text{O}_4$  nanocrystals only. Theoretical thermodynamic Wulff shape of the spinel crystallites was previously investigated by Zasada et al. [62]. Basing on the calculated surface energies of the exposed planes ((100) – 1.45 J m<sup>-2</sup>, (111) – 1.50, J m<sup>-2</sup>, A-(110) – 1.66 J m<sup>-2</sup>, and B-(110) – 1.89 J m<sup>-2</sup>), those authors predicted an equilibrium rhombicuboctahedral morphology of  $\text{Co}_3\text{O}_4$  that is almost equally dominated by the (111) and (100) facets (47.7% and 42.7%, respectively), with only minor contribution of the (110) plane (9.60 %). Despite the fact that the cobalt spinel nanocrystals are not of a model shape, owing to the constancy of the interfacial angles (Steno law), the inclinations of the malformed planes are the same as for the well-developed terminations. Hence, they may be used for reliable shape assignment within the

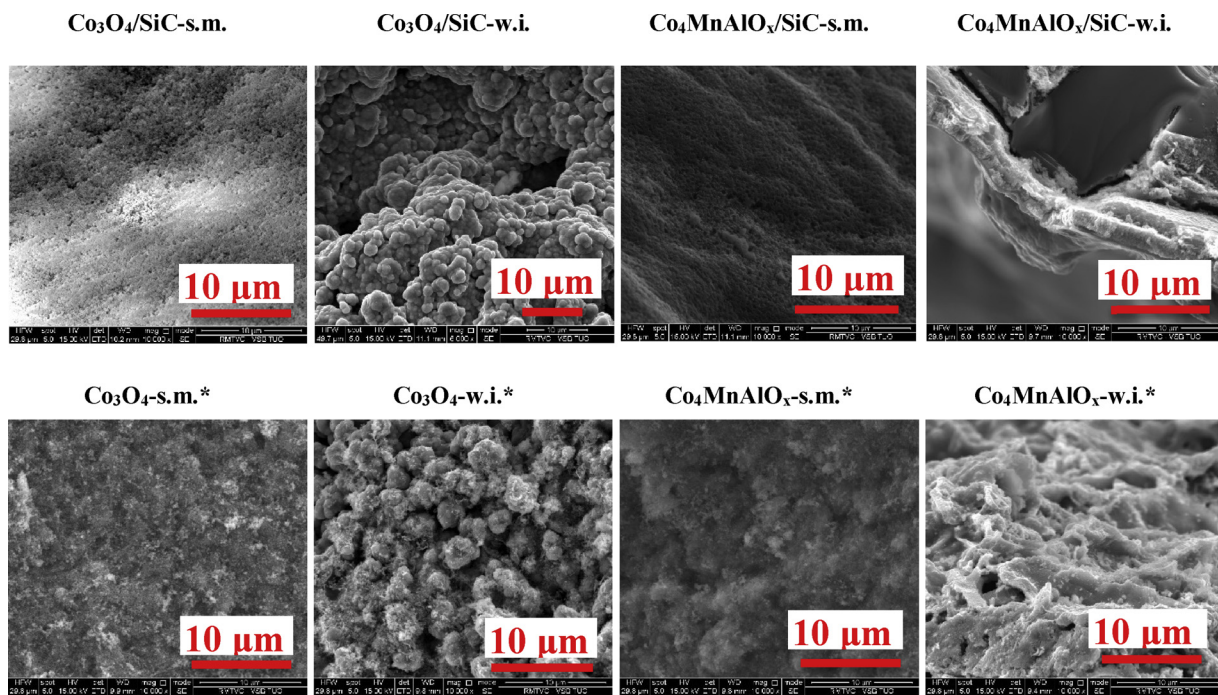
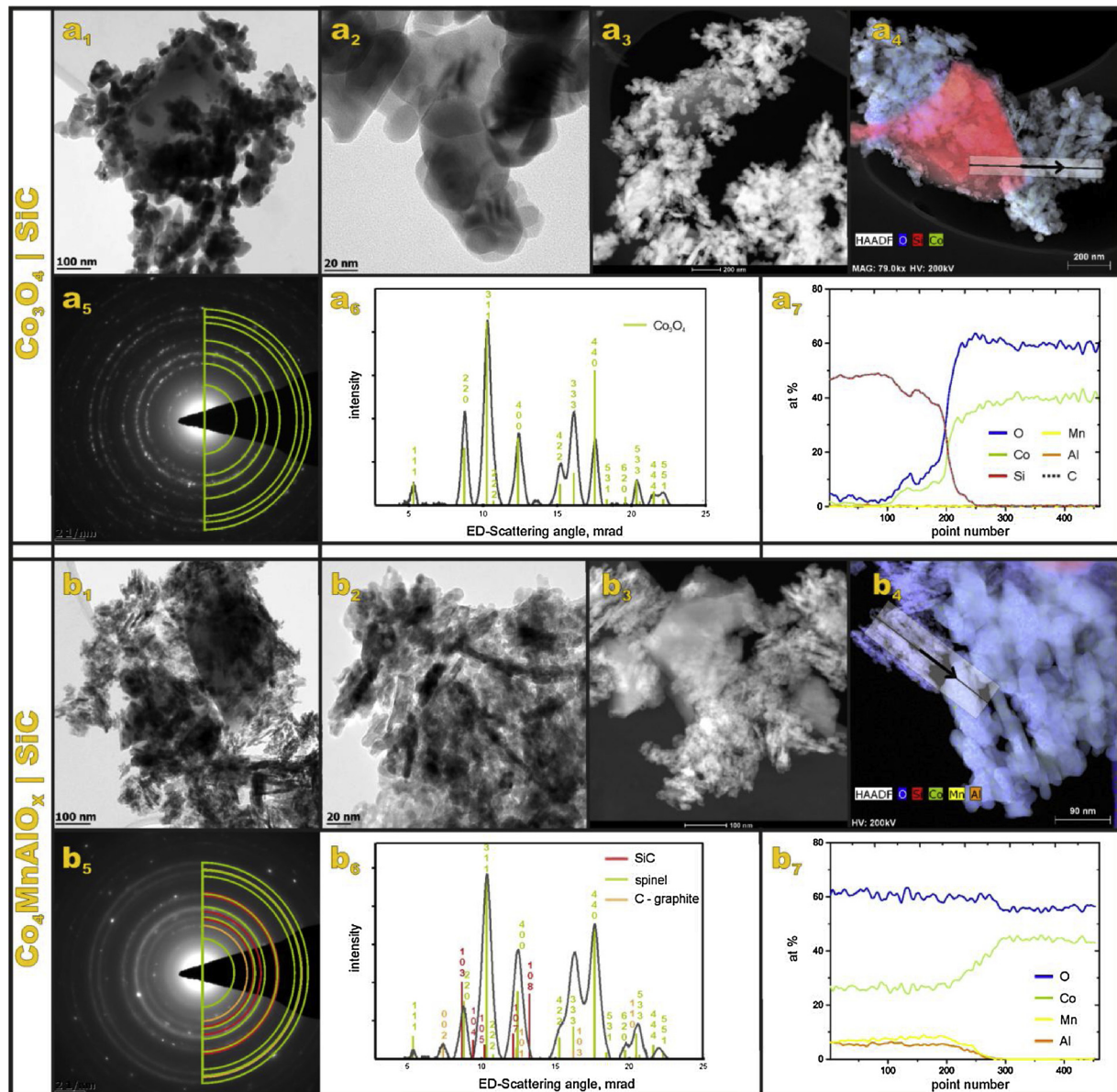


Fig. 3. SEM micrographs of the prepared foam catalysts and unsupported active phases. \*Determined on powder obtained by drying and calcination of parent suspension/solution.



**Fig. 4.** TEM (a<sub>1</sub>-a<sub>2</sub>, b<sub>1</sub>-b<sub>2</sub>) and STEM (a<sub>3</sub>, b<sub>3</sub>) overview images of Co<sub>3</sub>O<sub>4</sub> and Co-Mn-Al oxide nanoparticles in Co<sub>3</sub>O<sub>4</sub>/SiC-s.m and Co<sub>4</sub>MnAlO<sub>x</sub>/SiC-s.m. samples. STEM-HAADF images (a<sub>4</sub>, b<sub>4</sub>) superimposed with EDX chemical maps showing local distribution of the elements (K<sub>a</sub> - lines): O (blue), Co (green), Si (red), C (grey), Mn (yellow), Al (orange). Detail EDX line profile analysis (a<sub>7</sub>, b<sub>7</sub>) of a nanostructured assemblies confirms the nanoparticle stoichiometry. Polycrystalline electron diffraction patterns (a<sub>5</sub>, b<sub>5</sub>) with Debye-Scherrer half-ring overlays together with the radially integrated ring intensities (a<sub>6</sub>, b<sub>6</sub>) where the vertical markers indicate the peak positions of the identified crystallographic phases: Spinel (Fd3m) in green, SiC (P 63) in red, and C (P 63 mc) in orange.

polyhedral approximation.

The results of the shape analysis of the Co<sub>3</sub>O<sub>4</sub> nanocrystals are presented in Fig. 5 for Co<sub>3</sub>O<sub>4</sub>/SiC-s.m. and in Fig. 6 for Co<sub>4</sub>MnAlO<sub>x</sub>/SiC-s.m. Three representative morphologies of the cobalt spinel nanocrystals dispersed on the SiC foam are shown in Fig. 5. The first column presents the HAADF STEM images of the examined nanocrystals (Fig. 5a<sub>1</sub>-c<sub>1</sub>). The second column contains the analysis of the gradient HAADF STEM images, and is supplemented by investigation of the interplanar angles that are characteristic of the spinel structure (Fig. 5a<sub>2</sub>-c<sub>2</sub>). The third column presents the results of matching between the experimental HAADF STEM images and the projection of the proposed polyhedral shape onto the spinel nanocrystals. The retrieved morphologies are collated in the fourth column (Fig. 5a<sub>3</sub>-c<sub>3</sub>). The morphology analysis revealed that the spinel nanocrystals deposited on the silicon carbide support can be well described by the convex polyhedra with the interplanar angles equal to 109°, 125° and 144°

(Fig. 5a<sub>2</sub>-c<sub>2</sub>). In terms of the spinel structure, these angles are characteristic of the inter-junction between the (111)/(111), (111)/(100) and (111)/(110) facets, respectively. The morphology and the local orientation of the spinel nanocrystals presented in the first and the second row (Fig. 5a<sub>1</sub>-b<sub>4</sub>) implies characteristic changes of their thickness along the viewing direction, resulting in the corresponding changes of the images gradient. First, sharp change defines the edge of the nanocrystals. Then the slow decrease or increase in the gradient intensity, from the edge to the central part of the nanocrystals, indicate presence of the (100) and (111) facets, respectively.

The identified two type of cuboctahedral shapes are dominated by the (111) facets with abundance of 64 % or by the (100) facets with 72 % (Fig. 5a<sub>4</sub>, b<sub>4</sub>, respectively). A commonly observed feature for the Co<sub>3</sub>O<sub>4</sub> nanocrystals deposited on the SiC support is the junction between the nanocrystals, an example of which is shown in Fig. 5c<sub>1</sub>-c<sub>4</sub>. A more detailed analysis of the morphology (Fig. 5c<sub>1</sub>-c<sub>3</sub>) of such

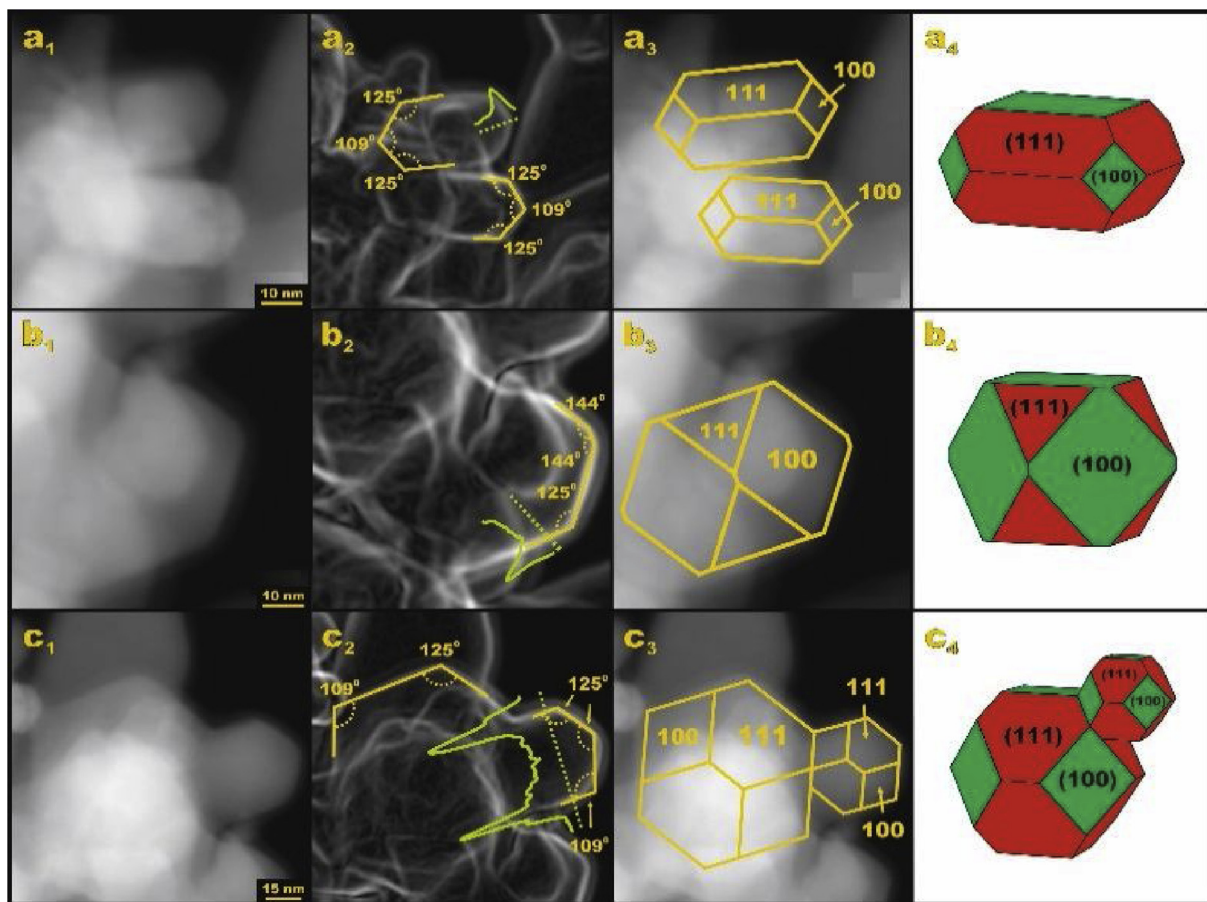


**Fig. 5.** HAADF STEM analysis of the morphologies of the  $\text{Co}_3\text{O}_4$  nanocrystals in  $\text{Co}_3\text{O}_4/\text{SiC-s.m.}$

a<sub>1</sub> – c<sub>1</sub>) HAADF STEM images of spinels deposited on the SiC foam.

a<sub>2</sub> – c<sub>2</sub>) Analysis of the HAADF STEM images gradient and the analysis of the interfacial angles characteristic of the spinel structure.

a<sub>3</sub> – c<sub>3</sub>) Matching between the experimental HAADF STEM images and the projections of the proposed polyhedral shape of the spinel nanocrystals.

a<sub>4</sub> – c<sub>4</sub>) Retrieved morphologies of the mixed spinel nanocrystals.

aggregates revealed their dicuboctahedral shape with the following abundance of the facets: 69 % (111)/31 % (100) for bigger and 65 % (111)/35 % (100) for smaller nanocrystals. A coherent junction between both moieties occurs via the (111)/(111) planes.

The results for the shape analysis of the segregated  $\text{Co}_3\text{O}_4$  nanocrystals present in the  $\text{Co}_4\text{MnAlO}_x/\text{SiC-s.m.}$  sample are shown in Fig. 6. The shape of these nanocrystals can be enclosed within the convex polyhedra with the interplanar angles equal to  $109^\circ$  and  $125^\circ$ , characteristic for the intersection between the (111)/(111) and (111)/(100)

facets, respectively. As described previously, the local orientation and the morphology impose distinctive changes of their thickness along the viewing direction, resulting in the corresponding changes in the images gradient, indicating the presence of the (100) and (111) facets. The resultant cuboctahedral shapes are presented in Fig. 6d. The both shapes are dominated by the (111) plane, with the following abundance of the facets: {56 % (111), 44 % (100)} and {64 % (111), 36 % (100)} for upper and lower shapes, respectively. Thus, they are similar in the morphology to the cobalt spinel nanocrystals observed previously for

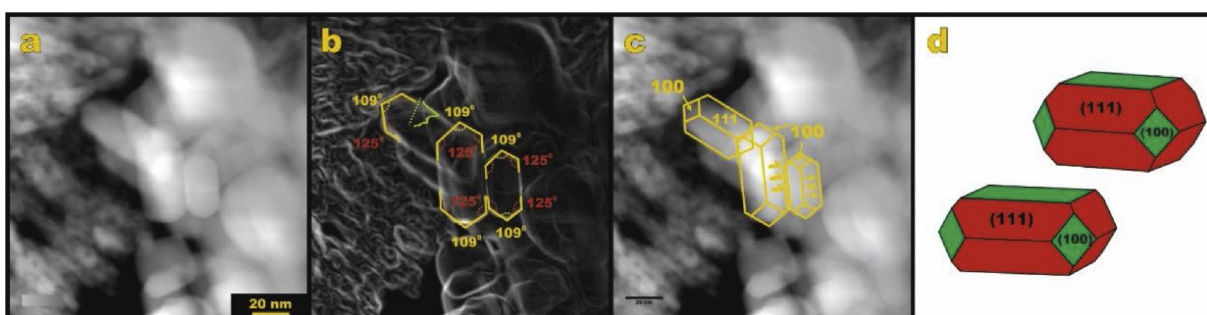


**Fig. 6.** HAADF STEM analysis of the morphologies of the  $\text{Co}_3\text{O}_4$  nanocrystals segregated from the mixed spinel phase in  $\text{Co}_4\text{MnAlO}_x/\text{SiC-s.m.}$

a) HAADF STEM image of the spinels deposited on the SiC foam.

b) Analysis of the HAADF STEM images gradient and the analysis of the interfacial angles characteristic of the spinel structure.

c) Matching between the experimental HAADF STEM images and the projections of the retrieved morphologies of the spinel nanocrystals.

a<sub>4</sub> – c<sub>4</sub>) Retrieved morphologies of the mixed spinel nanocrystals.

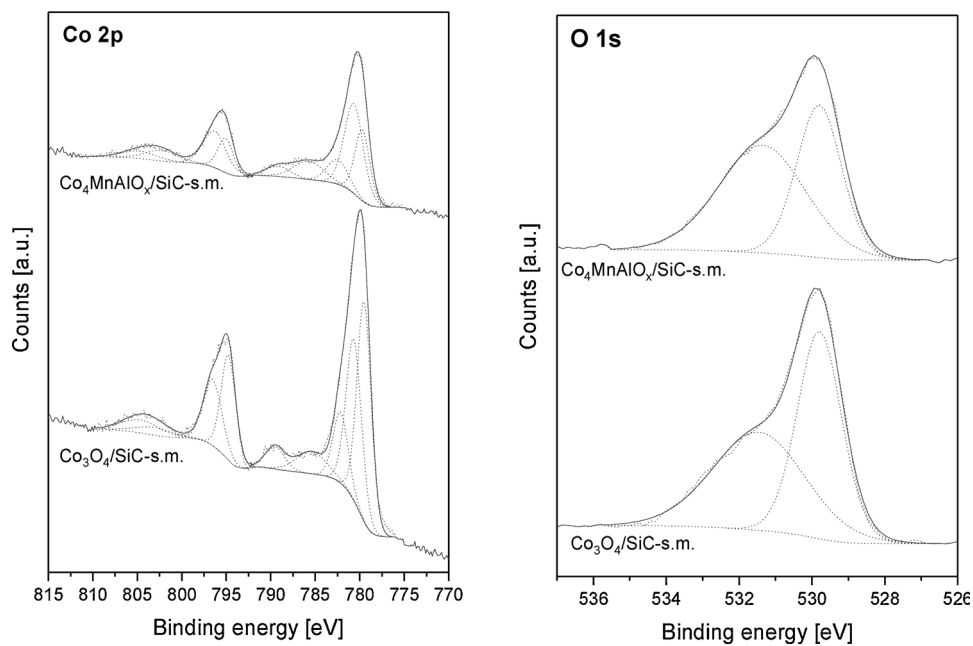


Fig. 7. XPS Co 2p and O 1s spectra of  $\text{Co}_3\text{O}_4/\text{SiC-s.m.}$  and  $\text{Co}_4\text{MnAlO}_x/\text{SiC-s.m.}$

the  $\text{Co}_3\text{O}_4/\text{SiC-s.m.}$  samples (cf. Fig. 5a<sub>1</sub>–a<sub>4</sub>).

The surface composition of the  $\text{Co}_3\text{O}_4/\text{SiC-s.m.}$  and  $\text{Co}_4\text{MnAlO}_x/\text{SiC-s.m.}$  samples was studied by XPS. Obviously, Co and O play a dominant role as elements present on the surface of  $\text{Co}_3\text{O}_4/\text{SiC-s.m.}$  In the Co 2p region (Fig. 7) two main photoemission maxima Co 2p<sub>3/2</sub> and Co 2p<sub>1/2</sub> (with the spin orbital splitting of 15.3 eV) together with satellite structure are observed. The deconvolution of Co 2p<sub>3/2</sub> peak confirms the presence of tetrahedral  $\text{Co}^{2+}$  (photoemission maximum at 780.7 eV accompanied by the component at 782.2 eV related to multiplet splitting of  $\text{Co}^{2+}$ ) and octahedral  $\text{Co}^{3+}$  (photoemission maximum at 779.5 eV), typical of the normal  $\text{Co}_3\text{O}_4$  spinel structure [63]. Furthermore, in the O 1s region (Fig. 7) the main peak attributed to lattice  $\text{O}^{2-}$  is found at 529.8 eV. Additionally, the presence of surface hydroxyls and chemisorbed oxygen is manifested by the peak at 531.5 eV [64].

In the XPS spectrum of the  $\text{Co}_4\text{MnAlO}_x/\text{SiC-s.m.}$  sample, the additional peaks related to photoemission from Mn and Al atoms appear (not shown). In the Al 2p region the single peak is centered at 74.2 eV. On the other hand, the Mn 2p<sub>3/2</sub> and Mn 2p<sub>1/2</sub> peaks can be deconvoluted into two components corresponding to  $\text{Mn}^{2+}$  (640.7 eV and 652.1 eV, respectively) and  $\text{Mn}^{4+}$  (642.8 eV and 653.3 eV, respectively) [65]. The calculated molar ratio of  $\text{Mn}^{2+}/\text{Mn}^{4+}$  is 1.8. The most interesting information on the surface composition of  $\text{Co}_4\text{MnAlO}_x/\text{SiC-s.m.}$  is however provided by the Co 2p region (Fig. 7). The components attributed to the  $\text{Co}_3\text{O}_4$  spinel phase (especially the peak at 779.7 eV due to octahedral  $\text{Co}^{3+}$ ) are still present, confirming the segregation of this phase observed in the STEM measurements. Nevertheless, the participation of  $\text{Co}^{2+}$  increases significantly and the molar ratio of  $\text{Co}^{2+}/\text{Co}^{3+}$  raises from 0.9 for  $\text{Co}_3\text{O}_4/\text{SiC-s.m.}$  to 1.6 for  $\text{Co}_4\text{MnAlO}_x/\text{SiC-s.m.}$  Moreover, an intensity of the satellite peaks increases dramatically. The more complex satellite structure observed for this sample can be explained by the appearance of octahedrally coordinated, high-spin  $\text{Co}^{2+}$  [66].

TPR-H<sub>2</sub> was used to characterize the reducibility of the prepared catalysts, since it is one of the main parameters which can govern oxide catalyst performance in redox reactions. TPR-H<sub>2</sub> results of deposited cobalt spinels and active phase obtained from parent solutions (bulk) were compared and are presented in Fig. 8 and Table 5. TPR-H<sub>2</sub> profiles show two main temperature regions (low temperature and high temperature) during reduction of  $\text{Co}_4\text{MnAlO}_x$  samples and just one (low temperature) region of  $\text{Co}_3\text{O}_4$  reduction.

For  $\text{Co}_3\text{O}_4$  sample, the low temperature peak obviously represents reduction of  $\text{Co}^{3+} \rightarrow \text{Co}^{2+} \rightarrow \text{Co}^0$  [10,54] in cobalt mixed oxide phase. Different TPR-H<sub>2</sub> profiles were obtained for  $\text{Co}_3\text{O}_4$  active phase obtained from parent solutions in grain form prepared from different precursors of  $\text{Co}_3\text{O}_4$ . Sample  $\text{Co}_3\text{O}_4$ -s.m. has two separated temperature maxima (341, 448 °C), but in case of  $\text{Co}_3\text{O}_4$ -w.i., the first temperature maximum is shifted to a higher temperature, coalescing with the second maximum (436 °C) and thus forming only a small shoulder at 380 °C. Different reducibility of  $\text{Co}_3\text{O}_4$  (one step or two-step reduction) can be connected with different crystallite sizes determined from XRD due to particle size effect reported in [67].

In the case of  $\text{Co}_4\text{MnAlO}_x$  sample, the reduction of  $\text{Mn}^{4+}$  to  $\text{Mn}^{3+}$  and  $\text{Mn}^{3+}$  to  $\text{Mn}^{2+}$  [53,68] can also take place theoretically in the low temperature region (220–450 °C) besides  $\text{Co}^{3+}$  and  $\text{Co}^{2+}$  reduction. Based on the TEM results, where the segregation of Co enriched  $\text{Co}_3\text{O}_4$  and mixed Co-Mn-Al oxide phase was visible, we can assume that cobalt species from local segregation of  $\text{Co}_3\text{O}_4$  in  $\text{Co}_4\text{MnAlO}_x$  sample are reduced in the low temperature region and the reduction of Co and Mn cations surrounded by Al ions in a spinel-like phase proceeds in the high temperature region [54,68]. Non-homogeneity of chemical composition as well as particle sizes in segregated Co-Mn-Al mixed oxide (according to TEM and SEM EDX analysis) led to wide character of reduction patterns of  $\text{Co}_4\text{MnAlO}_x$  sample.

After deposition of active phase on SiC foam, temperature maxima of all  $\text{Co}_3\text{O}_4$  and  $\text{Co}_4\text{MnAlO}_x$  samples shifted to higher temperatures. In the case of a samples with  $\text{Co}_3\text{O}_4$ , the first temperature maximum ( $\text{Co}_3\text{O}_4$ -s.m., 341 °C) and shoulder ( $\text{Co}_3\text{O}_4$ -w.i. 388 °C) are shifted to a higher temperature after deposition on support, coalescing with the second maxima (440–455 °C); temperatures of second maxima are comparable. This fact indicates deterioration of reducibility of  $\text{Co}^{3+}$  cobalt species after deposition on the SiC support especially for the sample prepared by suspension method. In the case of supported  $\text{Co}_4\text{MnAlO}_x$ , reducibility of hardly reducible components in high temperature region (> 500 °C) was not affected, but there are changes in the low temperature region. First maxima of both  $\text{Co}_4\text{MnAlO}_x$  samples on the SiC foam are wider and could be separated into two parts with maxima about 377 °C, which is comparable with first maximum of grain sample, and main maxima at higher temperatures (420 °C–433 °C), which may indicate a slight deterioration in reducibility of both samples.

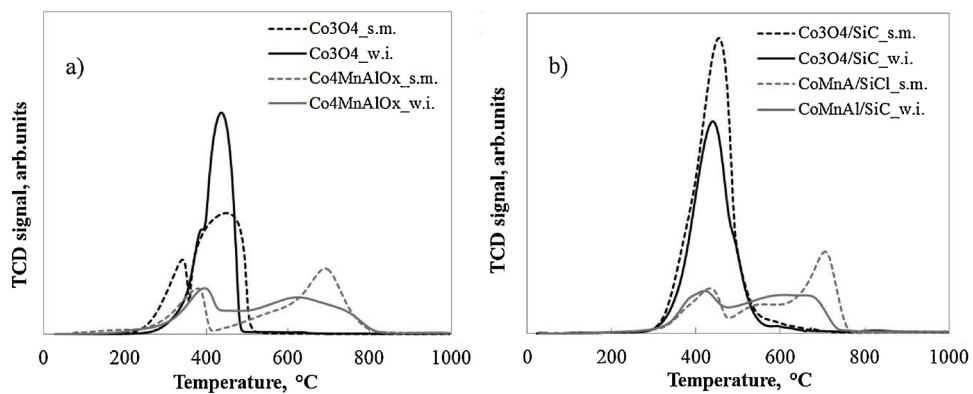


**Fig. 8.** TPR-H<sub>2</sub> of active phases a) in powder form prepared from parent solutions and b) deposited on SiC foams (crushed and sieved to fraction < 0.2 mm) and converted to amount of active phase on the support.

**Table 5**  
Results of TPR-H<sub>2</sub> on structured catalysts and active phase in powder form.

Catalyst	T <sub>max</sub> , °C	H <sub>2</sub> consumption, mmol/g (20-1000 °C)
Co <sub>3</sub> O <sub>4</sub> -s.m.	341, 448	19.0
Co <sub>3</sub> O <sub>4</sub> -w.i.	388, 436	19.9
Co <sub>4</sub> MnAlO <sub>x</sub> -s.m.	379, 691	14.7
Co <sub>4</sub> MnAlO <sub>x</sub> -w.i.	395, 623	14.2
Co <sub>3</sub> O <sub>4</sub> /SiC-s.m.	455	4.5
Co <sub>3</sub> O <sub>4</sub> /SiC-w.i.	440	3.5
Co <sub>4</sub> MnAlO <sub>x</sub> /SiC-s.m.	433, 565, 706	1.8
Co <sub>4</sub> MnAlO <sub>x</sub> /SiC-w.i.	420, 607	1.6

Worse reducibility of supported catalysts may be ascribed to the reduction of the metal-support species such as cobalt silicate species during TPR procedure. Those species can be easily formed between the hydroxides of SiO<sub>2</sub>, possibly present on the surface, and water ligands of metal salts during catalyst preparation, these can remain on the catalyst after calcination, and are hardly reducible at low temperatures but are undetectable by XRD [69]. Another possible explanation may be differences in microstructure which can be connected with repeated deposition of catalyst layer during catalysts preparation leading to worse access of cobalt and manganese species.

Interestingly, after deposition of both active phases on the SiC support, the differences in reducibility between samples prepared by different methods were minimized in comparison to unsupported samples, especially in the case of Co<sub>3</sub>O<sub>4</sub>.

Samples containing Co<sub>3</sub>O<sub>4</sub> active phase prepared by both methods either bulk or deposited on SiC possess higher amounts of reducible components (Table 5) in comparison with Co<sub>4</sub>MnAlO<sub>x</sub> containing samples which is in correlation with results of chemical analysis.

### 3.2. N<sub>2</sub>O catalytic decomposition

The temperature dependences of N<sub>2</sub>O conversion in inert atmosphere over active phase in grain form prepared from parent solution (bulk samples) is shown in Fig. 9a) and catalytic activity of cobalt mixed oxides deposited on SiC foams by different methods is shown in Fig. 9b).

Bulk samples prepared from hydroxide or hydrotalcite precursors (solutions for suspension method) show higher activity compared to those prepared from nitrates (solutions for wet impregnation). This is in good agreement with characterization results: using nitrates precursors for the preparation of cobalt oxides led to increase in crystallite size corresponding to their worse reducibility, lower specific surface areas and lower catalytic activity. The same finding was also confirmed in work [13]. It can be concluded that N<sub>2</sub>O conversions over active phase in grain form are almost independent on its chemical composition, the

samples containing Co<sub>3</sub>O<sub>4</sub> revealed almost comparable activity in comparison with Co<sub>4</sub>MnAlO<sub>x</sub> mixed oxide prepared by the same method.

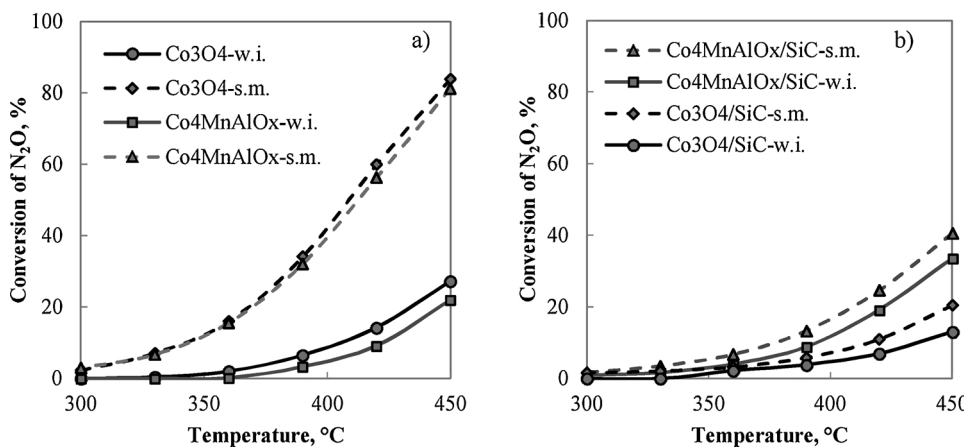
Conversion order changed after active phase deposition on SiC foam. Both catalysts containing Co<sub>4</sub>MnAlO<sub>x</sub> mixed oxide revealed higher conversion of N<sub>2</sub>O than those containing Co<sub>3</sub>O<sub>4</sub>. Moreover, the differences between conversions of all foam coated samples are smaller (29 % of absolute conversion) than differences in conversion of bulk samples (60 % of absolute conversion). It means that deposition procedure induced some changes responsible for the catalyst activity.

Since the active layer's thickness is lower than the size of grains used for measurement of bulk samples, we suppose that in the foam samples there are no internal diffusion limitation effects and activity change caused by the deposition procedure must have another reasons. The two main possible reasons are (i) interaction of active phase with support material and (ii) effect of geometrical re/arrangement of the active phase, which is related to different density of catalyst layers in cobalt spinel. Both of these reasons can change the reducibility of the resulting active phase, which was proven by TPR-H<sub>2</sub> and in turn influence catalytic activity. From the obtained characterization, as well as catalytic activity results, it can be concluded that active phase deposited by wet impregnation method is considerably more resistant against changes induced by deposition on the SiC support.

For unsupported samples in grain form the comparison of the two methods shown that suspension method produces active phase with higher surface areas and sites with better reducibility. Both of these factors contribute to higher N<sub>2</sub>O conversions. On the other hand, the reducibility of active phase prepared by suspension method after deposition on the SiC foams was greatly worsened in comparison to samples prepared by impregnation method. Moreover, these samples are susceptible to the mechanical deterioration, since the deposited layer is much more cracked than a layer deposited by impregnation method.

STEM analysis, XPS and TPR-H<sub>2</sub> confirmed presence of segregated Co<sub>3</sub>O<sub>4</sub> phase in Co<sub>4</sub>MnAlO<sub>x</sub>/SiC-s.m. observed by other techniques also in our previous works [54]. This segregated phase can contribute to catalytic activity of Co<sub>4</sub>MnAlO<sub>x</sub>/SiC-s.m. due to the fact the reduction of this Co<sub>3</sub>O<sub>4</sub> phase proceeds in the similar temperature region as N<sub>2</sub>O catalytic decomposition. According to literature [70,71], (100) facets in Co<sub>3</sub>O<sub>4</sub> spinel are more active for N<sub>2</sub>O catalytic decomposition in comparison to (111) and (110) planes. Our results are in agreement with this statement, since the shape analysis of Co<sub>3</sub>O<sub>4</sub> nanocrystals segregated in the most active Co<sub>4</sub>MnAlO<sub>x</sub>/SiC-s.m. showed the presence of cubooctahedral shapes with abundance of active (100) planes (36-44 %). However, according to high catalytic activity of Co<sub>4</sub>MnAlO<sub>x</sub> samples it is highly probable that besides Co<sub>3</sub>O<sub>4</sub> also abundant unfaceted grains of Co-Mn-Al oxide nanoparticles takes place in catalytic reaction.

In order to compare the catalytic activity of foam catalyst with



conventional fixed bed, the catalytic activity was also compared with active phase formed into pellet form by specific kinetic constants  $k$  (related to the unit of active phase) calculated according to:

$$k = \ln\left(\frac{1}{1 - X_{N_2O}}\right) / \frac{w_{\text{active phase}}}{V} \quad (1)$$

Where  $k$  ( $\text{m}^3 \text{kg}^{\text{active phase}}^{-1} \text{s}^{-1}$ ) is specific kinetic constant,  $X_{N_2O}$  (-) is conversion of  $\text{N}_2\text{O}$ ,  $w_{\text{active phase}}$  (kg) is weight of  $\text{Co}_3\text{O}_4$  or  $\text{Co}_4\text{MnAlO}_x$  and  $V$  ( $\text{m}^3 \text{s}^{-1}$ ) is volume flow.

Catalyst pellets were prepared from  $\text{Co}(\text{OH})\text{-}\beta$  and  $\text{Co}_4\text{MnAl}(\text{OH})_x(\text{CO}_3)_y$  precursors, which were calcined and formed to the pellet with size 5 x 5 mm. Temperature dependence of specific kinetic constants is presented on the Fig. 10. Deposition of active phase on the SiC foam support led to higher  $k$  of the active phase in comparison to pelleted catalyst in both cases ( $\text{Co}_3\text{O}_4$  and  $\text{Co}_4\text{MnAlO}_x$ ). Obtained results show that active phase deposited on the open-cell foam support could be good alternative to classical catalyst bed and it is promising for industrial applications, but requires further optimization. In future research, the catalytic activity of cobalt based active phase deposited on the foam support could be significantly increased by alkali promoters and also by optimization of amount of active phase on the support.

#### 4. Conclusions

Cobalt based mixed oxide ( $\text{Co}_3\text{O}_4$  or  $\text{Co}_4\text{MnAlO}_x$ ) was deposited on SiC foams by two different methods: wet impregnation and suspension method. Spinel phase was the only phase identified in all prepared catalysts.

$\text{Co}_3\text{O}_4$  and  $\text{Co}_4\text{MnAlO}_x$  deposited on the SiC foam by suspension

method were compared by TEM and XPS analysis. The obtained results revealed that the synthesis conditions of the spinel oxide play a role for both the particle morphology and its structural and chemical homogeneity. In case of  $\text{Co}_3\text{O}_4/\text{SiC-s.m.}$  sample despite being enclosed within (111) and (100) facets only, the morphology of the cobalt spinel nanocrystals vary from strongly prevailing abundance of (111) facet to the shape dominated by the (100) termination, preserving almost equal contribution of both type of nanocrystals shape within the sample population. A very similar shape was also observed for the  $\text{Co}_3\text{O}_4$  nanocrystals separated from the  $\text{Co}_4\text{MnAlO}_x/\text{SiC-s.m.}$  sample. The morphology of the Co-Mn-Al oxide nanoparticles is dominated by very small un-faceted grains, assembled into elongated fiber-like agglomerates.

Different structural properties and morphology led to different catalytic activity. Both foam samples containing  $\text{Co}_4\text{MnAlO}_x$  mixed oxide revealed higher conversion of  $\text{N}_2\text{O}$  than those containing  $\text{Co}_3\text{O}_4$ . Deposition of active phase from suspension solution led to (i) higher surface area of active phase; (ii) formation of thicker catalyst layer with uniform morphology; (iii) catalyst layer cracking, which can cause active phase loss during manipulation; (iv) higher catalytic activity in  $\text{N}_2\text{O}$  decomposition. Deposition of active phase from nitrate solution by impregnation led to (i) lower surface area of active phase; (ii) formation of thin, smooth surface without cracks and partial pore blocking; (iii) lower catalytic activity of  $\text{N}_2\text{O}$  decomposition in comparison with suspension method. Deposition of active phase on the SiC foam support led to higher specific kinetic constant of the active phase in comparison to pelleted catalyst in both cases ( $\text{Co}_3\text{O}_4$  and  $\text{Co}_4\text{MnAlO}_x$ ).

Obtained results show that active phase deposited on the open-cell foam support could be good alternative to classical catalyst bed and it is

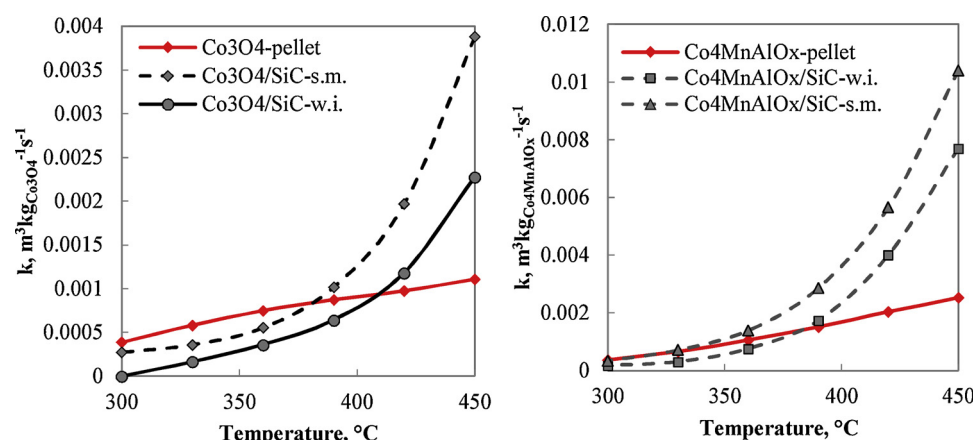


Fig. 10. Temperature dependence of specific kinetic constant of a)  $\text{Co}_3\text{O}_4$  deposited on the SiC foam and  $\text{Co}_3\text{O}_4$  in pelleted form, b)  $\text{Co}_4\text{MnAlO}_x$  deposited on the SiC foam and  $\text{Co}_4\text{MnAlO}_x$  in pelleted form.

promising for industrial applications, since deposition of active phase on the SiC foam support led to higher kinetic constant of the active phase in comparison to pelleted catalyst in both cases ( $\text{Co}_3\text{O}_4$  and  $\text{Co}_4\text{MnAlO}_x$ ).

## Acknowledgements

The work was supported from ERDF OP RDE "Institute of Environmental Technology – Excellent Research" No. CZ.02.1.01/0.0/0.0/16\_019/0000853 and OP RDI CZ.1.05/2.1.00/19.0389 "Research Infrastructure Development of the CENET".

## Appendix A. Supplementary data

Supplementary material related to this article can be found, in the online version, at doi:<https://doi.org/10.1016/j.apcatb.2019.117745>.

## Reference

[1] J. Pérez-Ramírez, F. Kapteijn, K. Schöffel, J.A. Moulijn, Formation and control of  $\text{N}_2\text{O}$  in nitric acid production: Where do we stand today? *Applied Catalysis B: Environmental* 44 (2003) 117–151.

[2] G. Maniak, P. Stelmachowski, F. Zasada, W. Piskorz, A. Kotarba, Z. Sojka, Guidelines for optimization of catalytic activity of 3d transition metal oxide catalysts in  $\text{N}_2\text{O}$  decomposition by potassium promotion, *Catalysis Today* 176 (2011) 369–372.

[3] C. Ohnishi, K. Asano, S. Iwamoto, K. Chikama, M. Inoue, Preparation of  $\text{Co}_3\text{O}_4$  Catalysts for Direct Decomposition of Nitrous Oxide under Industrial Conditions, in: M.D.D.E.D.V.S.H.P.A.J.J.A.M.E.M. Gaigneaux, P. Ruiz (Eds.), *Studies in Surface Science and Catalysis*, Elsevier, 2006, pp. 737–744.

[4] W. Piskorz, F. Zasada, P. Stelmachowski, A. Kotarba, Z. Sojka, Decomposition of  $\text{N}_2\text{O}$  over the surface of cobalt spinel: A DFT account of reactivity experiments, *Catalysis Today* 137 (2008) 418–422.

[5] N. Russo, D. Fino, G. Saracco, V. Specchia,  $\text{N}_2\text{O}$  catalytic decomposition over various spinel-type oxides, *Catal. Today* 119 (2007) 228–232.

[6] Ž. Chromáková, L. Obalová, F. Kovanda, D. Legut, A. Titov, M. Ritz, D. Fridrichová, S. Michalík, P. Kuštrawski, K. Jirátová, Effect of precursor synthesis on catalytic activity of  $\text{Co}_3\text{O}_4$  in  $\text{N}_2\text{O}$  decomposition, *Catal. Today* 257 (Part 1) (2015) 18–25.

[7] G. Grzybek, P. Stelmachowski, S. Gudyka, P. Indyka, Z. Sojka, N. Guillén-Hurtado, V. Rico-Pérez, A. Bueno-López, A. Kotarba, Strong dispersion effect of cobalt spinel active phase spread over ceria for catalytic  $\text{N}_2\text{O}$  decomposition: The role of the interface periphery, *Applied Catalysis B: Environmental* 180 (2016) 622–629.

[8] G. Grzybek, S. Wójcik, P. Legutko, J. Grybos, P. Indyka, B. Leszczyński, A. Kotarba, Z. Sojka, Thermal stability and repartition of potassium promoter between the support and active phase in the  $\text{K}-\text{Co}_{2.6}\text{Zn}_{0.4}\text{O}_4|\alpha\text{-Al}_2\text{O}_3$  catalyst for  $\text{N}_2\text{O}$  decomposition: Crucial role of activation temperature on catalytic performance, *Applied Catalysis B: Environmental* 205 (2017) 597–604.

[9] S. Kannan, Decomposition of nitrous oxide over the catalysts derived from hydrotalcite-like compounds, *Applied Clay Science* 13 (1998) 347–362.

[10] L. Obalová, K. Jirátová, F. Kovanda, K. Pacultová, Z. Lačný, Z. Mikulová, Catalytic decomposition of nitrous oxide over catalysts prepared from  $\text{Co}/\text{Mg}/\text{Mn}/\text{Al}$  hydrotalcite-like compounds, *Applied Catalysis B: Environmental* 60 (2005) 289–297.

[11] J. Pérez-Ramírez, J. Overeijnder, F. Kapteijn, J.A. Moulijn, Structural promotion and stabilizing effect of Mg in the catalytic decomposition of nitrous oxide over calcined hydrotalcite-like compounds, *Applied Catalysis B: Environmental* 23 (1999) 59–72.

[12] L. Obalová, K. Karásková, K. Jirátová, F. Kovanda, Effect of potassium in calcined Co–Mn–Al layered double hydroxide on the catalytic decomposition of  $\text{N}_2\text{O}$ , *Applied Catalysis B: Environmental* 90 (2009) 132–140.

[13] A. Klyushina, K. Pacultová, K. Karásková, K. Jirátová, M. Ritz, D. Fridrichová, A. Volodarskaja, L. Obalová, Effect of preparation method on catalytic properties of Co–Mn–Al mixed oxides for  $\text{N}_2\text{O}$  decomposition, *Journal of Molecular Catalysis A: Chemical* 425 (2016) 237–247.

[14] L. Obalová, K. Karásková, A. Wach, P. Kustrowski, K. Mamulová-Kutláková, S. Michalík, K. Jirátová, Alkali metals as promoters in Co–Mn–Al mixed oxide for  $\text{N}_2\text{O}$  decomposition, *Applied Catalysis A: General* 462–463 (2013) 227–235.

[15] B.M. Abu-Zied, S.A. Soliman, S.E. Abdellah, Enhanced direct  $\text{N}_2\text{O}$  decomposition over  $\text{Cu}_x\text{Co}_{1-x}\text{Co}_2\text{O}_4$  ( $0.0 \leq x \leq 1.0$ ) spinel-oxide catalysts, *J. Ind. Eng. Chem.* 21 (2015) 814–821.

[16] M. Inger, P. Kowalik, M. Saramok, M. Wilk, P. Stelmachowski, G. Maniak, P. Granger, A. Kotarba, Z. Sojka, Laboratory and pilot scale synthesis, characterization and reactivity of multicomponent cobalt spinel catalyst for low temperature removal of  $\text{N}_2\text{O}$  from nitric acid plant tail gases, *Catalysis Today* 176 (2011) 365–368.

[17] L. Obalová, K. Jirátová, K. Karásková, Ž. Chromáková,  $\text{N}_2\text{O}$  catalytic decomposition – From laboratory experiment to industry reactor, *Catalysis Today* 191 (2012) 116–120.

[18] M. Inger, M. Wilk, M. Saramok, G. Grzybek, A. Grodzka, P. Stelmachowski, W. Makowski, A. Kotarba, Z. Sojka, Cobalt Spinel Catalyst for  $\text{N}_2\text{O}$  Abatement in the Pilot Plant Operation–Long-Term Activity and Stability in Tail Gases, *Industrial & Engineering Chemistry Research* 53 (2014) 10335–10342.

[19] G. Grzybek, P. Stelmachowski, P. Indyka, M. Inger, M. Wilk, A. Kotarba, Z. Sojka, Cobalt–zinc spinel dispersed over cordierite monoliths for catalytic  $\text{N}_2\text{O}$  abatement from nitric acid plants, *Catalysis Today* 257 (Part 1) (2015) 93–97.

[20] R. Zhang, K. Hedjazi, B. Chen, Y. Li, Z. Lei, N. Liu, M(Fe, Co)-BEA washcoated honeycomb cordierite for  $\text{N}_2\text{O}$  direct decomposition, *Catalysis Today* 273 (2016) 273–285.

[21] S. Wójcik, G. Grzybek, J. Grybos, A. Kotarba, Z. Sojka, Designing, optimization and performance evaluation of the  $\text{K}-\text{Zn}_{0.4}\text{Co}_{2.6}\text{O}_4|\alpha\text{-Al}_2\text{O}_3$  cordierite catalyst for low-temperature  $\text{N}_2\text{O}$  decomposition, *Catalysis Communications* 110 (2018) 64–67.

[22] S. Wójcik, G. Ercolino, M. Gajewska, C.W.M. Quintero, S. Specchia, A. Kotarba, Robust  $\text{Co}_3\text{O}_4|\alpha\text{-Al}_2\text{O}_3$  cordierite structured catalyst for  $\text{N}_2\text{O}$  abatement – Validation of the SCS method for active phase synthesis and deposition, *Chemical Engineering Journal* (2018).

[23] L. del Río, G. Marbán, Stainless steel wire mesh-supported potassium-doped cobalt oxide catalysts for the catalytic decomposition of nitrous oxide, *Applied Catalysis B: Environmental* 126 (2012) 39–46.

[24] A. Klyushina, K. Pacultová, S. Krejčová, G. Slowik, K. Jirátová, F. Kovanda, J. Ryczkowski, L. Obalová, Advantages of stainless steel sieves as support for catalytic  $\text{N}_2\text{O}$  decomposition over K-doped  $\text{Co}_3\text{O}_4$ , *Catalysis Today* 257 (Part 1) (2015) 2–10.

[25] S. Gudyka, G. Grzybek, J. Grybos, P. Indyka, B. Leszczyński, A. Kotarba, Z. Sojka, Enhancing the  $\text{deN}_2\text{O}$  activity of the supported  $\text{Co}_3\text{O}_4|\alpha\text{-Al}_2\text{O}_3$  catalyst by glycerol-assisted shape engineering of the active phase at the nanoscale, *Applied Catalysis B: Environmental* 201 (2017) 339–347.

[26] G. Grzybek, S. Wójcik, K. Ciura, J. Grybos, P. Indyka, M. Oszajca, P. Stelmachowski, S. Witkowski, M. Inger, M. Wilk, A. Kotarba, Z. Sojka, Influence of preparation method on dispersion of cobalt spinel over alumina extrudates and the catalyst  $\text{deN}_2\text{O}$  activity, *Applied Catalysis B: Environmental* 210 (2017) 34–44.

[27] K. Pacultová, K. Karásková, J. Strakošová, K. Jirátová, L. Obalová, Supported Co–Mn–Al mixed oxides as catalysts for  $\text{N}_2\text{O}$  decomposition, *Comptes Rendus Chimie* 18 (2015) 1114–1122.

[28] K. Karásková, Ž. Chromáková, S. Študentová, V. Matějka, K. Jirátová, L. Obalová, A comparative study of  $\text{TiO}_2$ -supported and bulk Co–Mn–Al catalysts for  $\text{N}_2\text{O}$  decomposition, *Catalysis Today* 191 (2012) 112–115.

[29] Q. Shen, L. Li, J. Li, H. Tian, Z. Hao, A study on  $\text{N}_2\text{O}$  catalytic decomposition over  $\text{Co}/\text{MgO}$  catalysts, *Journal of Hazardous Materials* 163 (2009) 1332–1337.

[30] H.M. Choi, S.-J. Lee, S.-H. Moon, T.N. Phan, S.G. Jeon, C.H. Ko, Comparison between unsupported mesoporous  $\text{Co}_3\text{O}_4$  and supported  $\text{Co}_3\text{O}_4$  on mesoporous silica as catalysts for  $\text{N}_2\text{O}$  decomposition, *Catalysis Communications* 82 (2016) 50–54.

[31] M. Sahik, A. Tyagi, K. Killi, S. Challapalli, Catalytic decomposition of  $\text{N}_2\text{O}$  over  $\text{CeO}_2$  supported  $\text{Co}_3\text{O}_4$  catalysts, (2016).

[32] J. Ludvíková, K. Jirátová, J. Klempa, V. Boehmová, L. Obalová, Titania supported Co–Mn–Al oxide catalysts in total oxidation of ethanol, *Catalysis Today* 179 (2012) 164–169.

[33] E. Tronconi, G. Groppi, C.G. Visconti, Structured catalysts for non-adiabatic applications, *Current Opinion in Chemical Engineering* 5 (2014) 55–67.

[34] S.T. Kolaczkowski, S. Awdry, T. Smith, D. Thomas, L. Torkuhl, R. Kolvenbach, Potential for metal foams to act as structured catalyst supports in fixed-bed reactors, *Catalysis Today* 273 (2016) 221–233.

[35] P.H. Ho, M. Ambrosetti, G. Groppi, E. Tronconi, R. Palkovits, G. Fornasari, A. Vaccari, P. Benito, Chapter 15 – Structured Catalysts-Based on Open-Cell Metallic Foams for Energy and Environmental Applications, in: S. Albonetti, S. Perathoner, E.A. Quadrelli (Eds.), *Studies in Surface Science and Catalysis*, Elsevier, 2019, pp. 303–327.

[36] M.V. Twigg, J.T. Richardson, Structured ceramic foams as catalyst supports for highly exothermic processes, in: M.D.D.E.D.V.S.H.P.A.J.J.A.M.E.M. Gaigneaux, P. Ruiz (Eds.), *Studies in Surface Science and Catalysis*, Elsevier, 2006, pp. 135–142.

[37] A. Inayat, H. Freund, T. Zeiser, W. Schwieger, Determining the specific surface area of ceramic foams: The tetrakaidecahedra model revisited, *Chemical Engineering Science* 66 (2011) 1179–1188.

[38] J.T. Richardson, Y. Peng, D. Remue, Properties of ceramic foam catalyst supports: pressure drop, *Applied Catalysis A: General* 204 (2000) 19–32.

[39] E.A. Moreira, M.D.M. Innocentini, J.R. Coury, Permeability of ceramic foams to compressible and incompressible flow, *Journal of the European Ceramic Society* 24 (2004) 3209–3218.

[40] M. Lacroix, P. Nguyen, D. Schweich, C. Pham Huu, S. Savin-Poncet, D. Edouard, Pressure drop measurements and modeling on  $\text{SiC}$  foams, *Chemical Engineering Science* 62 (2007) 3259–3267.

[41] G. Incera Garrido, F.C. Patcas, S. Lang, B. Kraushaar-Czarnetzki, Mass transfer and pressure drop in ceramic foams: A description for different pore sizes and porosities, *Chemical Engineering Science* 63 (2008) 5202–5217.

[42] B. Dietrich, W. Schabel, M. Kind, H. Martin, Pressure drop measurements of ceramic sponges—Determining the hydraulic diameter, *Chemical Engineering Science* 64 (2009) 3633–3640.

[43] M.V. Twigg, J.T. Richardson, Preparation and properties of ceramic foam catalyst supports, in: J.M.B.D.P.A.J.G. Poncelet, P. Grange (Eds.), *Studies in Surface Science and Catalysis*, Elsevier, 1995, pp. 345–359.

[44] K. Jirátová, L. Morávková, J. Malecha, B. Koutský, Ceramic foam in catalytic combustion of methane, *Collection of Czechoslovak chemical communications* 60 (1995) 473–481.

[45] A. Schlegel, S. Buser, P. Benz, H. Bockhorn, F. Mauss, NO x formation in lean premixed noncatalytic andcatalytically stabilized combustion of propane, *Symposium (International) on Combustion*, Elsevier, 1994, pp. 1019–1026.

[46] P.S. Roy, C.S. Park, A.S.K. Raju, K. Kim, Steam-biogas reforming over a metal-foam-coated (Pd–Rh)/(CeZrO<sub>2</sub>–Al<sub>2</sub>O<sub>3</sub>) catalyst compared with pellet type alumina-supported Ru and Ni catalysts, *Journal of CO<sub>2</sub> Utilization* 12 (2015) 12–20.

[47] P.S. Roy, J. Song, K. Kim, J.-M. Kim, C.S. Park, A.S.K. Raju, Effects of CeZrO<sub>2</sub>–Al<sub>2</sub>O<sub>3</sub> support composition of metal-foam-coated Pd–Rh catalysts for the steam-biogas reforming reaction, *J. Ind. Eng. Chem.* 62 (2018) 120–129.

[48] X. Ou, F. Pilitsis, N. Xu, S.F.R. Taylor, J. Warren, A. Garforth, J. Zhang, C. Hardacre, Y. Jiao, X. Fan, On developing ferrisilicate catalysts supported on silicon carbide (SiC) foam catalysts for continuous catalytic wet peroxide oxidation (CWPO) reactions, *Catalysis Today* (2018).

[49] X. Ou, F. Pilitsis, Y. Jiao, Y. Zhang, S. Xu, M. Jennings, Y. Yang, S.F.R. Taylor, A. Garforth, H. Zhang, C. Hardacre, Y. Yan, X. Fan, Hierarchical Fe-ZSM-5/SiC foam catalyst as the foam bed catalytic reactor (FBCR) for catalytic wet peroxide oxidation (CWPO), *Chemical Engineering Journal* 362 (2019) 53–62.

[50] C.R. Thompson, P. Marín, F.V. Díez, S. Ordóñez, Evaluation of the use of ceramic foams as catalyst supports for reverse-flow combustors, *Chemical Engineering Journal* 221 (2013) 44–54.

[51] Y. Liu, D. Edouard, L.D. Nguyen, D. Begin, P. Nguyen, C. Pham, C. Pham-Huu, High performance structured platelet milli-reactor filled with supported cobalt open cell SiC foam catalyst for the Fischer–Tropsch synthesis, *Chemical Engineering Journal* 222 (2013) 265–273.

[52] V. Meille, Review on methods to deposit catalysts on structured surfaces, *Appl. Catal. A* 315 (2006) 1–17.

[53] L. Obalová, K. Pacultová, J. Balabánová, K. Jirátová, Z. Bastl, M. Valášková, Z. Lacný, F. Kovanda, Effect of Mn/Al ratio in Co–Mn–Al mixed oxide catalysts prepared from hydrotalcite-like precursors on catalytic decomposition of N<sub>2</sub>O, *Catalysis Today* 119 (2007) 233–238.

[54] F. Kovanda, T. Rojka, J. Dobešová, V. Machovič, P. Bezdička, L. Obalová, K. Jirátová, T. Grygar, Mixed oxides obtained from Co and Mn containing layered double hydroxides: Preparation, characterization, and catalytic properties, *Journal of Solid State Chemistry* 179 (2006) 812–823.

[55] D.R.G. Mitchell, B. Schaffer, Scripting-customised microscopy tools for Digital Micrograph(TM), *Ultramicroscopy* 103 (2005) 319–332.

[56] J.L. Lábár, M. Adamik, B.P. Barna, Z. Czígány, Z. Fogarassy, Z.E. Horváth, O. Geszti, F. Misák, J. Morgiel, G. Radnócz, G. Sáfrán, L. Székely, T. Szűts, Electron Diffraction Based Analysis of Phase Fractions and Texture in Nanocrystalline Thin Films, Part III: Application Examples, *Microscopy and Microanalysis* 18 (2012) 406–420.

[57] J. Canny, A Computational Approach to Edge Detection, *Readings in Computer Vision*, Morgan Kaufmann, San Francisco (CA), 1987, pp. 184–203.

[58] E. Meijering, J. Feature, Biomedical Imaging Group of the Swiss Federal Institute of Technology in Lausanne (EPFL), Switzerland, [www.imagescience.org/meijering/](http://www.imagescience.org/meijering/) software/featurej/.

[59] W.S. Rasband, ImageJ, U.S. National Institutes of Health Bethesda, Maryland, USA, 2014 [imagej.nih.gov/ij](http://imagej.nih.gov/ij).

[60] G. Wulff, *Zeitschrift für Krystallographie und Mineralogie*, (1901), pp. 449–530.

[61] F. Kapteijn, J.A. Moulijn, J. Weitkamp, J.A. Dalm, *Laboratory Reactors, Handbook of Heterogeneous Catalysis*, Wiley-VCH Verlag GmbH, 2008, pp. 1359–1398.

[62] F. Zasada, J. Gryboś, P. Indyka, W. Piskorz, J. Kaczmarczyk, Z. Sojka, Surface Structure and Morphology of M[CoM']O<sub>4</sub> (M = Mg, Zn, Fe, Co and M' = Ni, Al, Mn, Co) Spinel Nanocrystals—DFT + U and TEM Screening Investigations, *The Journal of Physical Chemistry C* 118 (2014) 19085–19097.

[63] A. Rokicinska, P. Natkanski, B. Dudek, M. Drodzak, L. Lityńska-Dobrzynska, P. Kustrowski, Co<sub>3</sub>O<sub>4</sub>-pillared montmorillonite catalysts synthesized by hydrogel-assisted route for total oxidation of toluene, *Applied Catalysis B-Environmental* 195 (2016) 59–68.

[64] S.C. Petitto, M.A. Langell, Surface composition and structure of Co<sub>3</sub>O<sub>4</sub>(110) and the effect of impurity segregation, *Journal of Vacuum Science & Technology A* 22 (2004) 1690–1696.

[65] O.A. Bulavchenko, Z.S. Vinokurov, T.N. Afonasenko, P.G. Tsyrl'nikov, S.V. Tsybulya, A.A. Saraev, V.V. Kachev, Reduction of mixed Mn-Zr oxides: in situ XPS and XRD studies, *Dalton Trans.* 44 (2015) 15499–15507.

[66] S.C. Petitto, E.M. Marsh, G.A. Carson, M.A. Langell, Cobalt oxide surface chemistry: The interaction of CoO(100), Co<sub>3</sub>O<sub>4</sub>(110) and Co<sub>3</sub>O<sub>4</sub>(111) with oxygen and water, *Journal of Molecular Catalysis a-Chemical* 281 (2008) 49–58.

[67] J. Kaczmarczyk, F. Zasada, J. Janas, P. Indyka, W. Piskorz, A. Kotarba, Z. Sojka, Thermodynamic Stability, Redox Properties, and Reactivity of Mn<sub>3</sub>O<sub>4</sub>, Fe<sub>3</sub>O<sub>4</sub>, and Co<sub>3</sub>O<sub>4</sub> Model Catalysts for N<sub>2</sub>O Decomposition: Resolving the Origins of Steady Turnover, *ACS Catalysis* 6 (2016) 1235–1246.

[68] K. Jirátová, J. Mikulová, J. Klempa, T. Grygar, Z. Bastl, F. Kovanda, Modification of Co–Mn–Al mixed oxide with potassium and its effect on deep oxidation of VOC, *Applied Catalysis A: General* 361 (2009) 106–116.

[69] N.O. Elbashir, P. Dutta, A. Manivannan, M.S. Seehra, C.B. Roberts, Impact of cobalt-based catalyst characteristics on the performance of conventional gas-phase and supercritical-phase Fischer–Tropsch synthesis, *Applied Catalysis A: General* 285 (2005) 169–180.

[70] F. Zasada, W. Piskorz, P. Stelmachowski, A. Kotarba, J.-F. Paul, T. Płociński, K.J. Kurzydłowski, Z. Sojka, Periodic DFT and HR-STEM Studies of Surface Structure and Morphology of Cobalt Spinel Nanocrystals. Retrieving 3D Shapes from 2D Images, *The Journal of Physical Chemistry C* 115 (2011) 6423–6432.

[71] F. Zasada, P. Stelmachowski, G. Maniak, J.-F. Paul, A. Kotarba, Z. Sojka, Potassium Promotion of Cobalt Spinel Catalyst for N<sub>2</sub>O Decomposition—Accounted by Work Function Measurements and DFT Modelling, *Catalysis Letters* 127 (2009) 126–131.